Journal of Materials Chemistry A

ROYAL SOCIETY OF CHEMISTRY

PAPER

View Article Online
View Journal | View Issue

Cite this: J. Mater. Chem. A, 2021, 9, 19949

Photo-assisted high performance single atom electrocatalysis of the N_2 reduction reaction by a Mo-embedded covalent organic framework†

Juan Wang,[a] Zhihua Zhang,[a] Siyun Qi,[a] Yingcai Fan,[a] Yanmei Yang,[b] Weifeng Li*[a] and Mingwen Zhao*[a]

Received 31st March 2021
Accepted 21st June 2021

DOI: 10.1039/d1ta02691g

rsc.li/materials-a

The development of highly efficient, low cost and environment-friendly solutions for the conversion of nitrogen gas to ammonia under ambient conditions has great industrial and academic significance. Single-atom catalysis (SAC) is recognized to have high potential in this area due to its rich chemical and physical properties. In this work, we proposed a Mo atom anchored covalent organic framework (MoPc-TFPN) for photo-assisted electrocatalysis of the N_2 reduction reaction using first-principles calculations. Our theoretical results demonstrated that this MoPc-TFPN catalyst has a considerably low onset potential of −0.24 V, which is comparable to or better than those of widely used noble catalysts. Because Mo denotes electrons to the Pc-TFPN substrate, the positive charged Mo has low binding affinity to H, thus greatly suppressing the competing hydrogen evolution reaction (HER). More importantly, the MoPc-TFPN has appropriate band edges with high light-absorption efficiency, which could be beneficial to improve the electrocatalytic efficiency of the NRR. This work uncovers a promising strategy for nitrogen fixation by photo-enhanced electrocatalysis under ambient conditions which could combine the ultimate functions of 2D semiconducting nanostructures for high performance catalysis.

1. Introduction

The conversion of gaseous nitrogen (N_2) to ammonia (NH_3) has high industrial significance.[1] However, the strong inertness of the N≡N bond makes the NH_3 production technically difficult.[2] Nowadays, the industrial NH_3 production mainly follows the traditional Haber–Bosch process. Using Fe- or Mo-based catalysts, N_2 and hydrogen (H_2) were circulated over the catalyst at a temperature of about 500 °C at a high pressure (150–350 atm) to produce NH_3.[3–5] The industrial-scale production of NH_3 faces the drawbacks of high energy consumption and low conversion rate. The development of economic and environment-friendly strategies to overcome these drawbacks of the Haber–Bosch method is highly desirable. In the biogeochemical nitrogen cycle, nitrogen fixation is catalyzed by an enzyme complex, nitrogenase, accounting for over 60% of the total atmospheric N_2 fixed.[6,7] Inspired by biological nitrogen fixation, heterogeneous catalysts through multiple proton and electron transfer steps for low energy consumption and zero CO_2 emission were proposed and have demonstrated big success.[8,9]

Currently, anchoring single-atom metals on the surface of 2D materials opened up a promising strategy to utilize the surface sites and improve the NRR process due to their high specific activity and maximum atom utilization. Furthermore, the positively charged metal atoms in SACs might be effective in suppressing the HER process by the coulombic interaction on the surface. SACs have been widely applied in a series of catalytic reactions,[10,11] *e.g.*, hydrogen evolution reaction (HER),[12] oxygen evolution reaction (OER),[13] oxygen reduction reaction (ORR),[14] NRR,[15] *etc.* Unfortunately, the high surface free energy of the anchored metal atoms results in migration and aggregation of active atoms during synthetic and catalytic processes, which leads to the rapid decay of catalytic activity.

With respect to SACs, two-dimensional covalent organic frameworks (2D-COFs) with porous configurations have drawn increasing interest, due to their high surface area, regular pore size, excellent electrical properties, tailorable structure and high stability.[16,17] A promising strategy to address the problem of active TM atom aggregation is to deposit TMs in 2D COFs.[18] Porous 2D COFs with modularly tunable structures assembled from metal cations and organic ligands hold great promise in gas sensors,[19] magnetism,[20] hyperbolic materials,[21] photo/electrocatalysts,[22,23] and so on. Especially, the porous configurations

[a]School of Physics & State Key Laboratory of Crystal Materials, Shandong University, Jinan 250100, Shandong, China. E-mail: lwf@sdu.edu.cn; zmw@sdu.edu.cn

[b]College of Chemistry, Chemical Engineering and Materials Science, Collaborative Innovation Center of Functionalized Probes for Chemical Imaging in Universities of Shandong, Key Laboratory of Molecular and Nano Probes, Ministry of Education, Shandong Normal University, Jinan, 250014, China

† Electronic supplementary information (ESI) available. See DOI: 10.1039/d1ta02691g

of 2D-COFs offer abundant sites to anchor TM atoms.[24] The π–π conjugation in 2D COFs can not only inhibit the aggregation of TM atoms and facilitate electron transportation in chemical reactions but also facilitates chemical reactions.[25] Very recently, Lan and co-workers reported the successful synthesis of dioxin-linked metallophthalocyanine covalent organic frameworks (MPc-TFPN COF) where the M represents Ni, Co or Zn.[26] Benefitting from the rich electrons of M atoms and efficient light absorption, electrocatalytic CO_2 reduction (ECR) was realized by the MPc-TFPN COF with remarkably high activity, stability and selectivity.

Numerous theoretical studies have highlighted the high NRR activity of 2D materials when anchored with Mo atoms, such as BN,[27] graphdiyne,[28] C_9N_4 (ref. 29) and 2D-COFs,[30,31] suggesting a promising strategy for the development of Mo-based NRR catalysts. Yang and co-workers have predicted the NRR performance of Mo atoms anchored on the BM-β_{12} monolayer with an onset potential of −0.26 V.[32] Motivated by the above reports, we anticipate that isolated Mo atoms anchored on the MPc-TFPN monolayer (MoPc-TFPN) would be a promising electrocatalyst for N_2 fixation in this work. In contrast to the easy-aggregation of Mo on the surface of graphene,[33] TM–N_4 can anchor stably on the MPc-TFPN and distribute evenly. Through first-principles calculations, we demonstrated that the MoPc-TFPN displays the highest NRR catalytic activity compared to all architectures reported before. The NRR onset potential is as low as 0.24 V, which is even lower than that of noble catalysts and COF-based catalysts. Our results also reveal that MoPc-TFPN has highly efficient optical absorption and large optical voltage which are the key features to drive the NRR process. In addition, the adsorption and activation of N_2 on MoPc-TFPN can be explained from the perspective of valence bond theory. This study provides a new and efficient approach for NRR photo-/electrocatalysts which could stimulate future experimental studies in this area.

2. Methods and computational details

Spin-polarized first-principles calculations were carried out on the basis of density functional theory (DFT) implemented in the Vienna *ab initio* simulation package (VASP) code to investigate the NRR on the MoPc-TFPN.[34,35] The electron–electron interaction was treated by the Perdew–Burke–Ernzerhof (PBE) style within the generalized gradient approximation (GGA).[36] Considering the porous configuration of the MoPc-TFPN, the van der Waals interaction was involved using the empirical correction in the Grimme's scheme (DFT-D3).[37] The projected augmented wave (PAW) potential[38] was utilized to describe the ion–electron interaction and the energy cutoff employed for plane-wave expansion of electron wave function in real space was set to 500 eV. The iterative convergences of energy and force were 10^{-5} eV and 0.01 eV $Å^{-1}$, respectively. An extra about 20 Å vacuum region was inserted along the *z*-direction to avoid mutual interaction between two periodic units. The Brillouin zone was sampled by a 3 × 3 × 1 *k*-point grid for electronic property calculation, whereas only the *Γ* point was considered in structural optimization. This *k*-point strategy has been verified to give sufficient accuracy. The HSE06 hybrid functional was utilized to calculate the electronic band structure and optical absorption spectrum. The thermal stability of the 2D MoPc-TFPN surface was studied by *Ab initio* Molecular Dynamics (AIMD) calculations at 800 K for 5000 fs. In addition, visualization analysis of charge density difference was performed by the VESTA code.[39] Taking into account that the NRR is conducted in aqueous electrolytes, the effects of aqueous solution were calculated with the implicit solvation model.[40]

The calculations of Gibbs free-energy change (ΔG) for each elemental step were based on the computational hydrogen electrode model proposed by Nørskov *et al.*,[41] which can be computed by

$$\Delta G = \Delta E + \Delta E_{ZPE} - T\Delta S - \Delta G_U + \Delta G_{pH}$$

where ΔE is the difference in reaction energy between products and reactants adsorbed on the catalyst surface obtained by using the DFT calculations, ΔE_{ZPE} is the zero-point energy difference between the adsorben and free molecules which can be evaluated from the vibration frequencies. T and S are the temperature and entropy, which can be found in the ESI.† $\Delta G_U = -eU$ in which U is defined relative to the SHE. $\Delta G_{pH} = k_B T \times \ln 10 \times pH$ is the correction of the free energy for H^+, where k_B is the Boltzmann constant. In our calculations, we took $T = 298.15$ K, $U = 0$ V and pH = 0. The detailed energetic characteristics for reaction intermediates are summarized in Tables S1 and S2 in the ESI.†

3. Results and discussion

3.1. Structure and stability of MoPc-TFPN

In experiments, the MPc-TFPN COF (M = Ni, Co, Zn) monolayers were synthesized by condensing 2,3,9,10,16,17,23,24-octahydroxyphthalocyaninato metal (MPc-8OH) with tetrafluorophthalonitrile (TFPN) to form three dioxin-linked phthalocyanine COFs[26] as shown in Fig. 1(a). The TM atoms are embedded in the framework by forming TM–N_4 units. In this work, we considered a specific MoPc-TFPN COF with Mo doping. To evaluate the structural stability, we defined the binding strength (E_b) between Mo and the Pc-TFPN framework as $E_b = E_{MoPc\text{-}TFPN} - E_{Mo} - E_{Pc\text{-}TFPN}$, with $E_{MoPc\text{-}TFPN}$, E_{Mo} and $E_{Pc\text{-}TFPN}$ depicting the energies of MoPc-TFPN, single Mo atoms and Pc-TFPN, respectively. After full structural optimization, it is found that the Mo atoms are firmly anchored onto the Pc-TFPN with E_b of −9.72 eV per Mo. For comparison, we also calculated the cohesive energy (E_{coh}) of the Mo metal using the definition: $E_{coh} = (E_{bulk} - n \times E_{Mo})/n$, where E_{bulk} represents the energy of the Mo crystal and n is the number of Mo atoms in the crystal. Using the same theoretical level of E_b, the E_{coh} of Mo is determined to be −6.89 eV per Mo, which is obviously higher than E_b. This implies that the interaction between Mo and Pc-TFPN is strong enough to avoid the self-aggregation of the anchored Mo atoms. By Bader charge analysis, about 1.47 electrons are transferred from each Mo atom to the Pc-TFPN COF, revealing the strong coupling of Mo to Pc-TFPN, which is conducive to enhancing Mo–N_4 bonds, thereby confirming

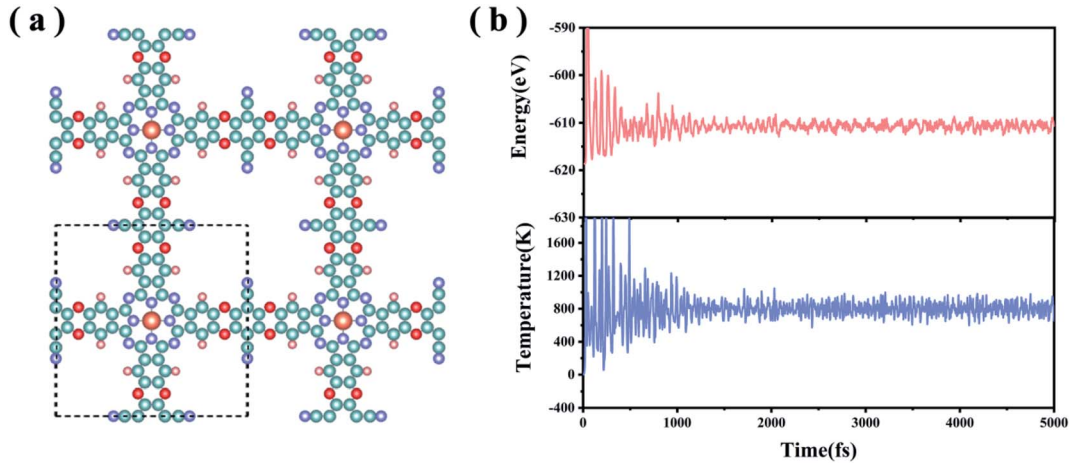

Fig. 1 (a) Top view of the atomic configuration of 2D MoPc-TFPN. The primitive cell is indicated by a black dotted square. The Mo, N, C, O and H atoms are represented by orange, purple, green, red and pink spheres, respectively. (b) Variations of energy and temperature during 5000 fs AIMD simulation.

the glorious structural stability of the MoPc-TFPN COF catalyst. To further verify the thermodynamic stability of MoPc-TFPN, *Ab initio* molecular dynamics simulations (AIMD) were conducted at a high temperature of 800 K for 5 ps with a time step of 1 fs, during which the total energy was monitored. As demonstrated in Fig. 1(b), the total energy quickly reached the equilibrium of −612 eV in about 1 ps and remained constant in the last simulations. Considerably small fluctuations are observed which is a direct indication of the high thermodynamic stability of MoPc-TFPN.

3.2. Chemisorption and activation of N_2

The first step of the NRR reaction is the chemisorption and activation of N_2 on the electrocatalyst. From our preliminary calculations, the ground state of MoPc-TFPN is spin-polarized and the spin is highly localized at the Mo atom with a magnetic moment of about 4 μ_B, which plays a vital role in N_2 activation. In addition, Bader charge analysis shows that 1.47 electrons are transferred from each Mo atom to the Pc-TFPN substrate, making the Mo atom highly positively charged and an ideal activation site for N_2 capture and activation. After

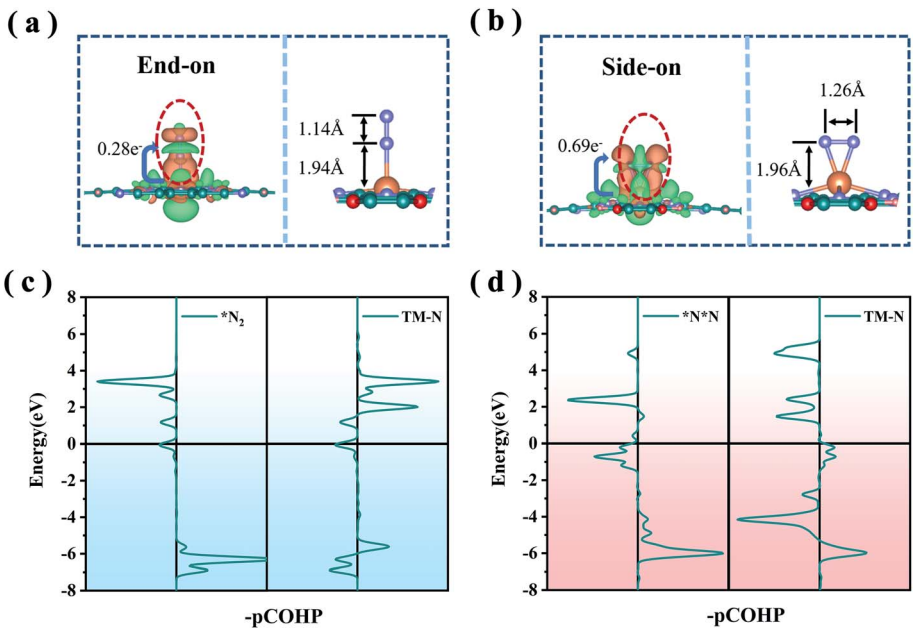

Fig. 2 Top and side views of the optimized configurations and the charge density difference of the N_2 molecule adsorbed on MoPc-TFPN adopting the (a) end-on pattern and (b) side-on pattern. The charge accumulation and depletion are displayed by the orange and green region. The projected crystal orbital Hamilton population (-pCOHP) of the N≡N bond and TM–N after adsorption of N_2 *via* the (c) end-on pattern and (d) side-on pattern.

structural optimization, two stable binding orientations were detected for the N_2 on the MoPc-TFPN surface which are denoted as end-on and side-on configurations as depicted in Fig. 2. The lengths of the Mo–N bonds for the end-on and side-on patterns are 1.94 and 1.96 Å, respectively. The free energies of N_2 adsorption are −0.55 eV (end-on) and −0.01 eV (side-on), indicating that the chemisorption of nitrogen is a spontaneous process from the gaseous N_2, especially for the end-on pattern. Significant charge transfer was observed between the anchored Mo atom and N_2 for both adsorption configurations. In detail, there are 0.28 and 0.64 electrons transferred to MoPc-TFPN for the end-on and side-on modes. This difference can be attributed to the higher amount of back-donation taking place in the side-on the than the end-on mode.[42] The charge redistribution can be visualized by the charge accumulation and depletion displayed by the orange and green region in Fig. 2(a) and (b), where the electron transfer in the side-on case is more obvious than the end-on case. Moreover, the stability of adsorbed N_2 is correlated with the occupancy of antibonding orbitals, as shown in Fig. 2(c). The antibonding orbitals of the side-on model are closer to the E_F compared with that of end-on, implying that the transferred electrons occupy the antibonding orbitals in the side-on mode. Furthermore, the integrated crystal orbital Hamilton population (ICOHP) values of the N≡N bond in the $*N_2$ intermediate are −7.05 and −3.19 for the end-on and side-on configurations, respectively.[43,44] All these results indicate that the end-on mode is energetically more favorable than the side-on binding mode.

The reaction of the N_2 adsorbate with the exposed Mo atom follows the "acceptance–donation" mechanism.[45] More specifically, as depicted in Fig. 3(c), the Mo atom at the center possessing the empty d orbital can "accept" the lone-pair electrons from the N_2 to strengthen the Mo–N bond, and meanwhile "donate" electrons to the antibonding orbitals of N_2 to weaken the N≡N bond. To verify the essential orbitals in the NRR reaction, each orbital of gaseous N_2 near the Fermi level (E_F), *i.e.*, 2σ, 2σ*, 2π, 3σ and 2π*, and the 3σ orbital is summarized in Fig. 3(a) which is represented as the partial density of states (PDOS). The unoccupied d orbitals of the Mo atom on the MoPc-TFPN accept electrons from the 2π and 3σ molecular orbitals of N_2, forming the bonding states to strengthen the N_2 adsorption and becoming metallic. Good electrical conductivity is the essential factor to improve the electrocatalytic performance of the NRR. Meanwhile, the occupied d orbitals donate electrons to the 2π* orbital of N_2, as shown by partial density of states (PDOS) in Fig. 3(a) and (b). Therefore, these electronic features make MoPc-TFPN a promising catalyst for the conversion of N_2 to NH_3.

3.3. Reaction pathway and free energy profile

As depicted in Fig. 4, the electrocatalytic nitrogen-to-ammonia conversion is a complicating process which includes two different N_2 adsorption configurations (end-on and side-on modes as shown in Fig. 2), four possible reaction pathways (distal, alternating, consecutive and enzymatic routes) and six proton/electron pair (H^+/e^-) reduction steps. In the following, we discuss these reaction pathways and the corresponding profiles of free energy Δ*G*. The model structures with top and side views of the whole process are shown in Fig. S1–S4 in the ESI.†

We firstly assessed the distal pathway and calculated the reaction energy profile shown in Fig. 5(a). For the first hydrogenation step ($*N_2 + *H \rightarrow *N_2H$), it is uphill by 0.24 eV due to the weak adsorption of N_2H* species. Subsequently, the third proton/electron pairs attack the distal N atom of $*N_2H_2$, breaking the N–N bond to release the first NH_3 molecule. The

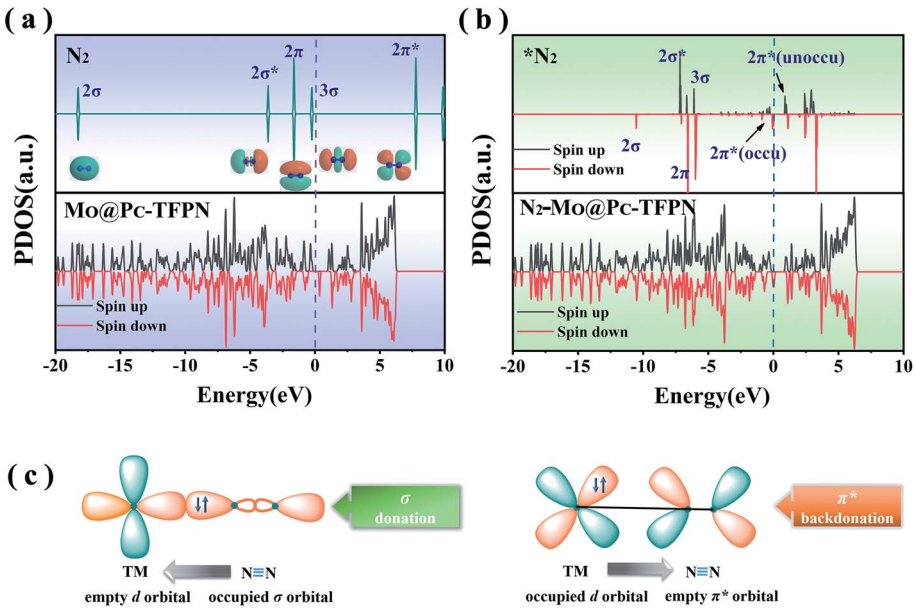

Fig. 3 (a) Partial density of states (PDOS) of the free N_2 molecule and isolated MoPc-TFPN surface. (b) The PDOS of the adsorbed N_2 molecule and N_2-MoPc-TFPN complex *via* the end-on pattern. (c) Schematic diagram of the N_2 molecule bonding to the Mo atom.

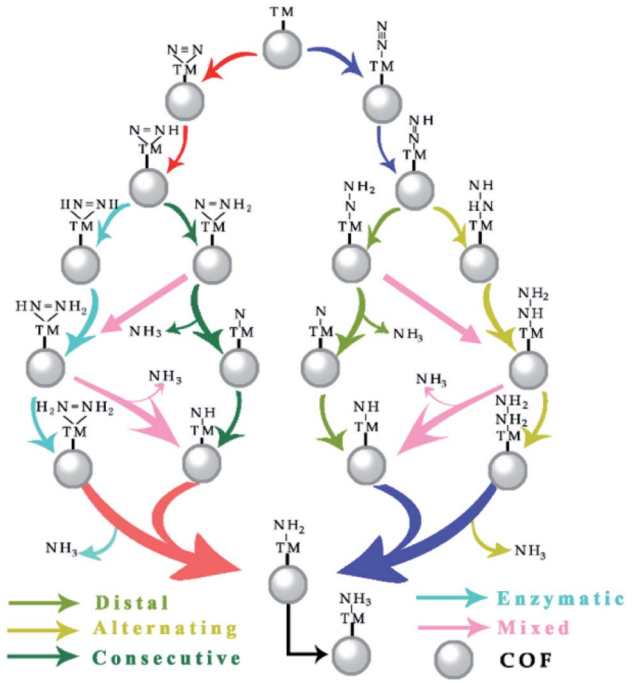

Fig. 4 Schematic depiction of four pathways for N_2 reduction to NH_3.

remaining *N is then hydrogenated to form *NH, *NH_2 and *NH_3 by successively adsorbing three proton/electron pairs. The hydrogenation of *N_2 to *N_2H has a Gibbs free energy barrier of only 0.24 eV. This value of hydrogenation is significantly lower than those of most of the TM-based SACs for the NRR reported so far and this hydrogenation reaction has been believed to be the potential-determining step (PDS).[46–48]

Additionally, we also investigated the alternating pathway (Fig. 5(b)). It is worth mentioning that the first two steps in the NRR are identical for the distal and the alternating pathways, *i.e.*, $N_2 \rightarrow *N_2$ and $*N_2 + *H \rightarrow *N_2H$. The protonation step of $*N_2H + *H \rightarrow *NHNH$ has the maximum change of Gibbs free energy of 0.72 eV. Subsequently, proton/electron pairs consecutively attack the N atoms to form *$NHNH_2$ and *NH_2NH_2 species, and meanwhile the N≡N bond is elongated but does not break, initiating the N_2 activation. Compared with the alternating mechanism, the NRR by the MoPc-TFPN monolayer *via* the distal mechanism is energetically favorable for the protonation steps of $*N_2H + *H \rightarrow *N_2H_2$ and $*N_2H_2 + *H \rightarrow *N + NH_3(g)$ as the free energies are calculated to be −0.26 and −1.38 eV, respectively. In the last step, the two nitrogen atoms are hydrogenated sequentially, releasing two ammonia molecules.

For the enzymatic pathway illustrated in Fig. 5(c), N_2 atoms bind to the catalyst surface in a side-on binding mode. Generally, the trend of the energy profile in the enzymatic pathway is similar to that of the alternating pathway. The adsorbed N_2 molecule is firstly hydrogenated by reaction with a $(H^+ + e^-)$ pair to produce *N*NH. After a series of hydrogenation steps, the *N*NH is successively reduced to *NH*NH, *NH*NH_2, *NH_2-*NH_2 and *NH_2 + $NH_3(g)$, with the corresponding values of ΔG being 0.42, 0.09, −0.67 and −1.90 eV, respectively. The free energy change in the first hydrogenation step ($*N_2 + *H \rightarrow$ *N*NH) is superior to the alternating pathway with a considerably small PDS of 0.25 V. However, from the perspective of the

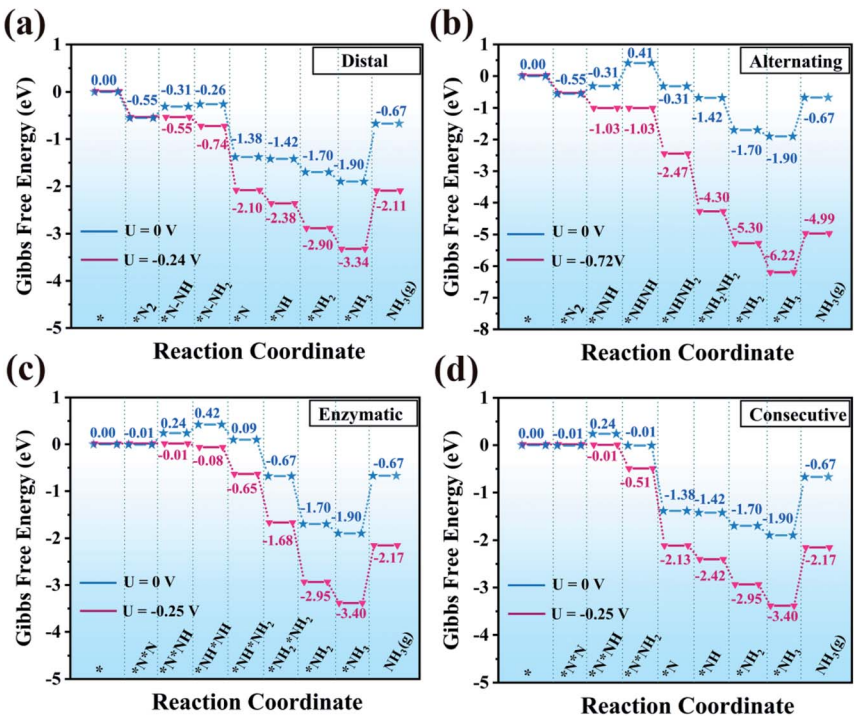

Fig. 5 Gibbs free energy diagrams for the NRR on MoPc-TFPN through (a) distal, (b) alternating, (c) enzymatic and (d) consecutive pathways in water solvent.

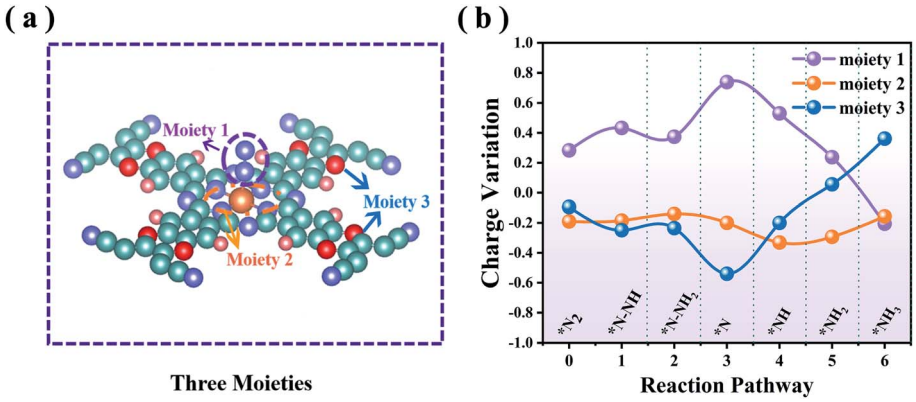

Fig. 6 (a) Schematic structures of the three moieties on MoPc-TFPN with NmHn adsorption. (b) The Bader charge variations of the three moieties along the distal reaction pathway. The charge variation starts from N_2 adsorption which is defined as step 0.

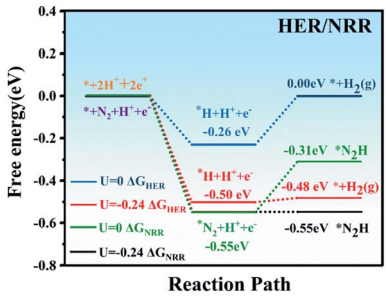

Fig. 7 Free energy diagram of the HER and NRR on MoPc-TFPN; $U = -0.24$ V is the NRR onset potential.

minimum energy principle, the enzymatic pathway is energetically unfavorable because nitrogen adsorption is more stable in end-on mode.

Finally, for the consecutive pathway in Fig. 5(d), the PDS is the hydrogenation of *N*N into *N*NH with a low free energy of 0.25 eV, which is endothermic while all the others are exothermic. The general trend of the energy profile in the last four steps (the formation and desorption of NH_3) is similar to that in the distal pathway. The rate-determining step of the four reaction pathways is the first hydrogenation process with a negligible onset potential difference. From all the above results, the low over-potential endows MoPc-TFPN with a high potential to act as a highly efficient catalyst for N_2 reduction into NH_3 with low energy consumption. Based on the above PDS and energy analysis, it is found that the distal reaction pathway is the most favorable pathway with a considerably low onset potential of −0.24 V relative to the SHE, which is superior to other recently proposed efficient SACs, such as single Pt atom supported on g-C_3N_4,[49] single-atom Fe implanted nitrogen-doped carbon catalysts (Fe_1-N-C)[50] and N-doped porous carbon.[51] It is noteworthy that *NH_3 → NH_3(g) showed an uphill energy change independent of the applied potential with a NH_3 desorption energy of 1.23 eV, which is disadvantageous for NH_3 release. However, in the experiments, the ammonia does not exist in the form of gaseous ammonia, but as protonated NH_4^+ ions.[52–54] It has also been proved that this step is actually not an obstacle because *NH_3 is prone to protonation to form NH_4^+ in the acidic electrolyte (pH = 0).[44,55] In addition, our predicted value (1.23 eV) is much lower than that of B@g-CN (2.23 eV)[56] and Pt-SACs/CTF (1.40 eV)[57] NRR catalysts. For comparison, the Pt-SACs/CTF nanosheets are experimentally reported to have excellent NRR photocatalytic performance and the potential of photogenerated electrons (−0.54 V) is sufficient to drive the NRR.[57] Therefore, the desorption of NH_3 from the MoPc-TFPN in the current study is expected to be not difficult.

Considering that the electrocatalytic NRR takes place in an aqueous environment,[58] we considered the solvation effects in our calculations by VASPsol. It is found that the solvation has different contributions to the energetic features of the intermediate, where the onset potential was lowered by ∼0.1 eV. Additionally, because the NRR process involves complicated surface–adsorbate interactions, enthalpy correction to the Gibbs free energy should be included, which is about 0.03–0.11 eV, consistent with the previous report.[47] The Gibbs free energy diagrams with and without the solvation and enthalpy corrections are summarized in Fig. S5.† It is seen that the Gibbs free energy change of the PDS for the distal NRR mechanism is reduced from 0.24 to 0.21 eV. Furthermore, the thermal corrections $\int C_p dT$ for each individual adsorbed species on Mo-TFPN are also calculated and given in Table S2.† Notably, the above corrections not only substantially changed Gibbs free energies but also altered the identity of the PDS.

3.4. Origin of the high NRR activity

To probe the mechanistic origin of the high catalytic activity of MoPc-TFPN, for each hydrogenation step we analyzed the charge transfer between the reactants. For the whole NRR process, each intermediate can be divided into three moieties:[56] N_mH_n (moiety 1), the MoN_4 unit composed of a Mo atom with four surrounding N atoms (moiety 2) and the Pc-TFPN ligand without N_4 (moiety 3), as illustrated in Fig. 6(a). From Fig. 6(b) and Table S3 in the ESI† we can see that the adsorbed N_mH_n can obtain electrons from the Pc-TFPN substrate during the N_2 adsorption, the first hydrogenation step and the *N–NH_3 formation. In the following, the redundant electrons of the

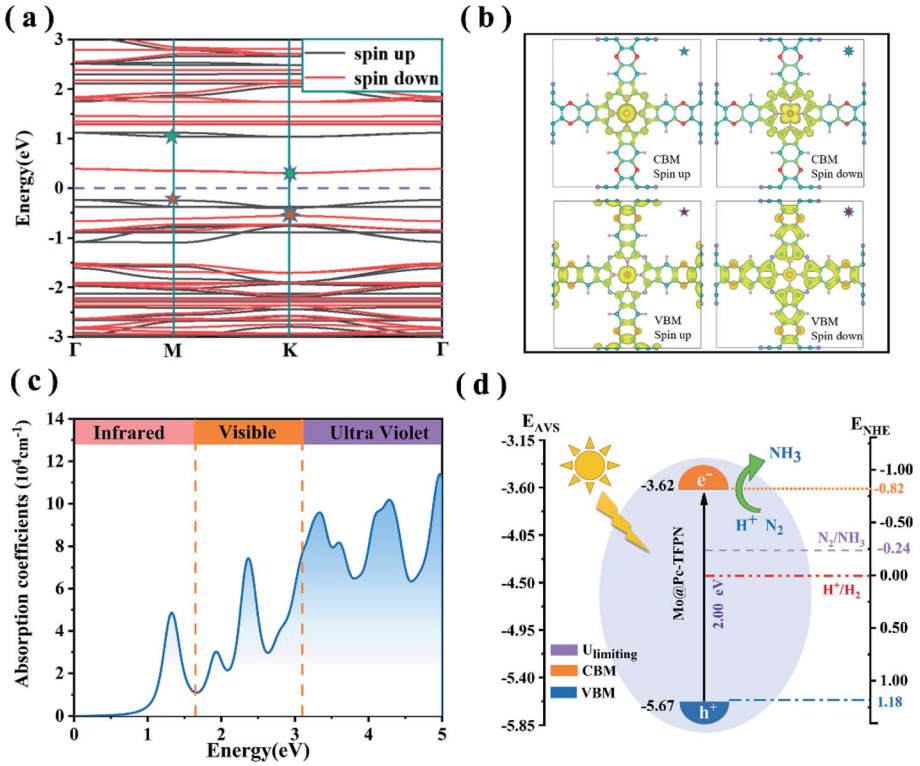

Fig. 8 (a)The spin-polarized band structures of the MoPc-TFPN monolayer from the PBE hybrid functional. The Fermi level is at zero. (b) The charge distributions of the Kohn–Sham electron wavefunctions of the VBM and CBM of the MoPc-TFPN monolayer. The isosurface value is 0.003 e Å^{-3}. (c)The optical absorption coefficients of the MoPc-TFPN monolayer using the HSE06 functional. (d) Schematic illustration of the band edge positions of MoPc-TFPN. E_{NHE} and E_{AVS} denote energy levels relative to the normal hydrogen electrode (NHE) at pH = 0 and the absolute vacuum scale (AVS), respectively.

N_mH_n transferred back to the substrate. Thus, the variations of the charges of moiety 1 and moiety 3 change in an opposite manner, while for the MoN_4 unit moiety, it mainly acts as an intermediary of electrons to translocate between the Pc-TFPN and N_mH_n species in the subsequent four hydrogenation processes, although a constant net charge of ~0.2 |e| is observed. As a consequence, efficient charge transfer to N_2 is recognized to be one essential factor to the enhanced NRR catalyst.

3.5. Selectivity of MoPc-TFPN for the NRR against HER

Ammonia selectivity against the hydrogen evolution reaction (HER) is another crucial criterion to evaluate the NRR catalytic performance, because the HER is considered to be a competing reaction to the NRR in acidic electrolytes.[59] Poor selectivity to ammonia will cause excessive hydrogen adsorption on the active sites, causing deactivation of the catalyst and inhibiting the two reactions. On the other hand, from a kinetic point of view, the combination of protons and electrons will generate H_2 instead of NH_3. Therefore, in the NRR reaction, it is of great significance to suppress the competing HER process.

Our calculations showed that the adsorption energy of a H atom on MoPc-TFPN is about −0.55 eV, which is considerably weaker than the binding of a N_2 molecule on MoPc-TFPN (−0.82 eV). This implies that the N_2 molecule has higher priority than H_2 to bind with MoPc-TFPN, which suppresses the subsequent HER. The specific values of ΔG_H and ΔG_{N_2} for MoPc-TFPN are determined to be −0.26 and −0.55 eV when $U = 0$ *vs.* SHE. It will lead to preferential coverage of N_2 molecules on the TM, instead of H. Moreover, the Gibbs free energy of H adsorption on the surface of MoPc-TFPN ($|\Delta G_H| = 0.26$ eV) is higher than the onset potential of the NRR (0.24 eV). Thus, when the electrode potential of −0.24 V is adopted, the NRR can proceed spontaneously along the distal pathway because the HER faces an energy barrier of about 0.02 eV as shown in Fig. 7. As a consequence, the MoPc-TFPN should exhibit a high NRR selectivity and suppressed HER. Additionally, the possible poisoning effects of H_2O molecules on the MoPc-TFPN catalyst have also been explicitly considered in our calculations, where the binding energy of a H_2O molecule on the Mo atom of MoPc-TFPN in the aqueous solution is only −0.36 eV, indicating that the presence of a H_2O molecule will not poison the catalyst.[30]

3.6. Optical performance of MoPc-TFPN

As revealed from experiments, light irradiation facilitates electrochemical activation of CO_2 molecules over the phthalocyanine COF catalyst because the current density increases under light irradiation.[26] Thus we anticipate that, for the phthalocyanine MoPc-TFPN under study, light irradiation can enhance the electron transfer to the adsorbed N_2, thus benefitting the reduction of N_2. The spin-polarized electron band structures of

the MoPc-TFPN are presented in Fig. 8(a). It is seen that the 2D MoPc-TFPN monolayer is an indirect band gap semiconductor with the band gaps of 1.39 and 1.00 eV for the two spin channels. As the PBE function always underestimates the band gap of semiconductors, the HSE06 function was used to verify the polarized gaps which gave the band gaps of 2.00 and 1.39 eV for spin-up and spin-down respectively. The electron–hole interactions also regulate the optical properties. Especially, numerous studies pointed out that pristine COF polymers usually have a high exciton binding energy which severely hinders the charge hole separation.[60,61] Fig. 8(b) depicts the spatial distributions of the electrons and holes in MoPc-TFPN where electrons and holes are effectively separated. In detail, the valence band maximum (VBM, the holes) states are localized at the ligand of the MoPc-TFPN, while the conduction band minimum (CBM, the electrons) states are mainly located at the Mo and N atoms of the inner side.

Light absorption ability is another key factor in the efficiency of photocatalysts.[62–65] To initiate the photocatalytic N_2 conversion to NH_3, the photocatalyst should possess a strong capability to harvest solar light, especially the ultraviolet and visible regions. Considering this, we further calculated the light absorption spectrum of MoPc-TFPN from the complex dielectric function calculated at the DFT-HSE06 level. As shown in Fig. 8(c), the MoPc-TFPN exhibits remarkable absorption in the visible light region and extends to infrared light. Moreover, the energies of the first absorption peak agree well with the band gap of 1.35 eV from the HSE06 function, validating the accuracy of the theoretical strategy employed in this work.

For photofixation of nitrogen, the ideal catalysts should have suitable band edges that match the N_2/NH_3 potentials.[57,66,67] Light irradiation can excite electrons from the VBM to the CBM which are further transferred to adsorbed N_2. As shown in Fig. 8(c), the negative conduction band position CBM (−0.82 V *vs.* NHE) of MoPc-TFPN is higher than the initial potential of N_2/NH_3 (−0.24 V *vs.* NHE), while for the VBM, it is located below the H^+/H_2 potential for the spin up bands. These results indicate that MoPc-TFPN has the capability of light absorption which can assist N_2 conversion under visible-light irradiation.[53]

Combining the three features of highly electron–hole separation, wide light absorption ranges and appropriate band edge positions, the MoPc-TFPN is theoretically predicted to have high solar conversion efficiency, which is believed to greatly assist the NRR reaction.

Besides MoPc-TFPN, we have also considered other 2D TMPc-TFPN COFs with TM = Sc–Zn, Ru, Rh, Pd, and Ag. Our calculations showed that, except Mo, these TMPc-TFPN COFs have either weak N_2 adsorption capability with positive ΔG_{N2} or large $\Delta G_{N2H} - \Delta G_{N2}$ values (>0.74 eV), thus resulting in low NRR catalytic activity. Therefore, only MoPc-TFPN stands out from the 2D TMPc-TFPN COFs as a promising NRR electrocatalyst.

4. Conclusions

To summarize, through first principles theory calculations, we rationally designed 2D MoPc-TFPN single-atom catalysts which exhibited remarkably high catalytic activity and excellent selectivity for the N_2 fixation and reduction reaction under ambient conditions. This catalyst has a considerably small onset potential of −0.24 V and follows the distal mechanism for the conversion of N_2 to NH_3. The onset potential is further reduced to −0.21 V when considering the enthalpy correction and solvation effect. The origin of the high NRR catalytic activity of MoPc-TFPN can be elucidated by the "acceptance–donation" mechanism. More importantly, the efficient electron–hole separation and appropriate band edges account for the high light-absorption of MoPc-TFPN, which could be beneficial to improve the electrocatalytic efficiency of the NRR by light irradiation. This work offers a rational design for advanced sustainable NH_3 production and can potentiate 2D semiconducting nanostructures for highly efficient catalysis.

Conflicts of interest

The authors declare no competing financial interest.

Acknowledgements

This study is supported by the National Natural Science Foundation of China (no. 11774201), the Natural Science Foundation of Shandong Province (ZR2020JQ04), and the Taishan scholarship of Shandong Province.

References

1 Y. Wan, J. Xu and R. Lv, *Mater. Today*, 2019, **27**, 69–90.
2 C. J. M. van der Ham, M. T. M. Koper and D. G. H. Hetterscheid, *Chem. Soc. Rev.*, 2014, **43**, 5183–5191.
3 A. Banerjee, B. D. Yuhas, E. A. Margulies, Y. Zhang, Y. Shim, M. R. Wasielewski and M. G. Kanatzidis, *J. Am. Chem. Soc.*, 2015, **137**, 2030–2034.
4 H. Li, J. Shang, Z. Ai and L. Zhang, *J. Am. Chem. Soc.*, 2015, **137**, 6393–6399.
5 C. Ling, Y. Zhang, Q. Li, X. Bai, L. Shi and J. Wang, *J. Am. Chem. Soc.*, 2019, **141**, 18264–18270.
6 D. E. Canfield, A. N. Glazer and P. G. Falkowski, *Science*, 2010, **330**, 192–196.
7 S. Sultana, S. Mansingh and K. M. Parida, *J. Mater. Chem. A*, 2019, **7**, 9145–9153.
8 H. Liu, L. Wei, F. Liu, Z. Pei, J. Shi, Z.-j. Wang, D. He and Y. Chen, *ACS Catal.*, 2019, **9**, 5245–5267.
9 Q. Li, Y. Guo, Y. Tian, W. Liu and K. Chu, *J. Mater. Chem. A*, 2020, **8**, 16195–16202.
10 M. Khalid, P. A. Bhardwaj, A. M. B. Honorato and H. Varela, *Catal. Sci. Technol.*, 2020, **10**, 6420–6448.
11 S. Qi, J. Wang, X. Song, Y. Fan, W. Li, A. Du and M. Zhao, *Sci. Bull.*, 2020, **65**, 995–1002.
12 Z. H. Zhang, S. Y. Qi, X. H. Song, J. Wang, W. Q. Zhang and M. W. Zhao, *Appl. Surf. Sci.*, 2021, **553**, 7.
13 W. Zhang, H. Bu, J. Wang, L. Zhao, Y. Qu and M. Zhao, *J. Mater. Chem. A*, 2021, **9**, 4221–4229.
14 H. Zhong, K. H. Ly, M. Wang, Y. Krupskaya, X. Han, J. Zhang, J. Zhang, V. Kataev, B. Buechner, I. M. Weidinger, S. Kaskel,

P. Liu, M. Chen, R. Dong and X. Feng, *Angew. Chem., Int. Ed.*, 2019, **58**, 10677–10682.
15 L. Li, J. M. P. Martirez and E. A. Carter, *ACS Catal.*, 2020, **10**, 12841–12857.
16 C. Yang, Z.-D. Yang, H. Dong, N. Sun, Y. Lu, F.-M. Zhang and G. Zhang, *ACS Energy Lett.*, 2019, **4**, 2251–2258.
17 J. Wang, J. R. Wang, X. H. Song, S. Y. Qi and M. W. Zhao, *Appl. Surf. Sci.*, 2020, **511**, 7.
18 J. Wang, J. Wang, S. Qi and M. Zhao, *J. Phys. Chem. C*, 2020, **124**, 17675–17683.
19 Z. Meng, R. M. Stolz and K. A. Mirica, *J. Am. Chem. Soc.*, 2019, **141**, 11929–11937.
20 I. E. Brumboiu, S. Haldar, J. Luder, O. Eriksson, H. C. Herper, B. Brena and B. Sanyal, *J. Chem. Theory Comput.*, 2016, **12**, 1772–1785.
21 H. Gao, X. Zhang, W. Li and M. Zhao, *Opt. Express*, 2019, **27**, 36911–36922.
22 X. Song, J. Wang, S. Qi, Y. Fan, W. Li and M. Zhao, *J. Phys. Chem. C*, 2019, **123**, 25651–25656.
23 Z. Zhang, S. Yang, M. Dou, H. Liu, L. Gu and F. Wang, *RSC Adv.*, 2016, **6**, 67049–67056.
24 Q.-L. Zhu, W. Xia, T. Akita, R. Zou and Q. Xu, *Adv. Mater.*, 2016, **28**, 6391.
25 P. Peng, L. Shi, F. Huo, S. Zhang, C. Mi, Y. Cheng and Z. Xiang, *ACS Nano*, 2019, **13**, 878–884.
26 M. Lu, M. Zhang, C.-G. Liu, J. Liu, L.-J. Shang, M. Wang, J.-N. Chang, S.-L. Li and Y.-Q. Lan, *Angew. Chem., Int. Ed.*, 2021, **60**, 4864–4871.
27 J. Zhao and Z. Chen, *J. Am. Chem. Soc.*, 2017, **139**, 12480–12487.
28 M. Li, Y. Cui, X. Zhang, Y. Luo, Y. Dai and Y. Huang, *J. Phys. Chem. Lett.*, 2020, **11**, 8128–8137.
29 X. Z. Zhe Xue, J. Qin and R. Liu, *J. Energy Chem.*, 2021, **57**, 443–450.
30 F. Liu, L. Song, Y. Liu, F. Zheng, L. Wang, K. Palotas, H. Lin and Y. Li, *J. Mater. Chem. A*, 2020, **8**, 3598–3605.
31 C. Wang, Y.-N. Zhao, C.-Y. Zhu, M. Zhang, Y. Geng, Y.-G. Li and Z.-M. Su, *J. Mater. Chem. A*, 2020, **8**, 23599–23606.
32 L. Xu, L. M. Yang and E. Ganz, *ACS Appl. Mater. Interfaces*, 2021, **13**, 14091–14101.
33 J. Long, X. Fu and J. Xiao, *J. Mater. Chem. A*, 2020, **8**, 17078–17088.
34 G. Kresse and J. Furthmuller, *Phys. Rev. B: Condens. Matter Mater. Phys.*, 1996, **54**, 11169–11186.
35 G. Kresse and J. Furthmuller, *Comput. Mater. Sci.*, 1996, **6**, 15–50.
36 J. P. Perdew, K. Burke and M. Ernzerhof, *Phys. Rev. Lett.*, 1996, **77**, 3865–3868.
37 S. Grimme, J. Antony, S. Ehrlich and H. Krieg, *J. Chem. Phys.*, 2010, **132**, 154104.
38 G. Kresse and D. Joubert, *Phys. Rev. B: Condens. Matter Mater. Phys.*, 1999, **59**, 1758–1775.
39 K. Momma and F. Izumi, *J. Appl. Crystallogr.*, 2011, **44**, 1272–1276.
40 K. Mathew, R. Sundararaman, K. Letchworth-Weaver, T. A. Arias and R. G. Hennig, *J. Chem. Phys.*, 2014, **140**, 084106.
41 J. K. Nørskov, J. Rossmeisl, A. Logadottir, L. Lindqvist, J. R. Kitchin, T. Bligaard and H. Jonsson, *J. Phys. Chem. B*, 2004, **108**, 17886–17892.
42 R. Kumar and A. K. Singh, *ChemCatChem*, 2020, **12**, 5456–5464.
43 S. Maintz, V. L. Deringer, A. L. Tchougreeff and R. Dronskowski, *J. Comput. Chem.*, 2016, **37**, 1030–1035.
44 X. Guo, J. Gu, S. Lin, S. Zhang, Z. Chen and S. Huang, *J. Am. Chem. Soc.*, 2020, **142**, 5709–5721.
45 X. Yang, C. Shang, S. Zhou and J. Zhao, *Nanoscale Horiz.*, 2020, **5**, 1106–1115.
46 C. Ren, Q. Jiang, W. Lin, Y. Zhang, S. Huang and K. Ding, *ACS Appl. Nano Mater.*, 2020, **3**, 5149–5159.
47 C.-X. Huang, G. Li, L.-M. Yang and E. Ganz, *ACS Appl. Mater. Interfaces*, 2021, **13**, 608–621.
48 C. Choi, S. Back, N.-Y. Kim, J. Lim, Y.-H. Kim and Y. Jung, *ACS Catal.*, 2018, **8**, 7517–7525.
49 H. Yin, S.-L. Li, L.-Y. Gan and P. Wang, *J. Mater. Chem. A*, 2019, **7**, 11908–11914.
50 R. Zhang, L. Jiao, W. Yang, G. Wan and H.-L. Jiang, *J. Mater. Chem. A*, 2019, **7**, 26371–26377.
51 Y. Liu, Y. Su, X. Quan, X. Fan, S. Chen, H. Yu, H. Zhao, Y. Zhang and J. Zhao, *ACS Catal.*, 2018, **8**, 1186–1191.
52 J. Zhang, X. Tian, M. Liu, H. Guo, J. Zhou, Q. Fang, Z. Liu, Q. Wu and J. Lou, *J. Am. Chem. Soc.*, 2019, **141**, 19269–19275.
53 Y. Shiraishi, M. Hashimoto, K. Chishiro, K. Moriyama, S. Tanaka and T. Hirai, *J. Am. Chem. Soc.*, 2020, **142**, 7574–7583.
54 Y. Ling, F. Kazim, S. Ma, Q. Zhang, K. Qu, Y. Wang, S. Xiao, W. Cai and Z. Yang, *J. Mater. Chem. A*, 2020, **8**, 12996–13003.
55 H. Niu, X. Wang, C. Shao, Z. Zhang and Y. Guo, *ACS Sustainable Chem. Eng.*, 2020, **8**, 13749–13758.
56 X. Lv, W. Wei, F. Li, B. Huang and Y. Dai, *Nano Lett.*, 2019, **19**, 6391–6399.
57 J. Li, P. Liu, Y. Tang, H. Huang, H. Cui, D. Mei and C. Zhong, *ACS Catal.*, 2020, **10**, 2431–2442.
58 H. Guo, L. Li, X. Wang, G. Yao, H. Yu, Z. Tian, B. Li and L. Chen, *ACS Appl. Mater. Interfaces*, 2019, **11**, 36506–36514.
59 X. Zhai, L. Li, X. Liu, Y. Li, J. Yang, D. Yang, J. Zhang, H. Yan and G. Ge, *Nanoscale*, 2020, **12**, 10035–10043.
60 C. Schweitzer and R. Schmidt, *Chem. Rev.*, 2003, **103**, 1685–1757.
61 N. C. Flanders, M. S. Kirschner, P. Kim, T. J. Fauvell, A. M. Evans, W. Helweh, A. P. Spencer, R. D. Schaller, W. R. Dichtel and L. X. Chen, *J. Am. Chem. Soc.*, 2020, **142**, 14957–14965.
62 Y. Fan, X. Song, S. Qi, X. Ma and M. Zhao, *J. Mater. Chem. A*, 2019, **7**, 26123–26130.
63 S. Qi, Y. Fan, J. Wang, X. Song, W. Li and M. Zhao, *Nanoscale*, 2020, **12**, 306–315.
64 Y. Fan, J. Wang and M. Zhao, *Nanoscale*, 2019, **11**, 14836–14843.
65 Y. Fan, X. Ma, X. Liu, J. Wang, H. Ai and M. Zhao, *J. Phys. Chem. C*, 2018, **122**, 27803–27810.
66 S. Bian, M. Wen, J. Wang, N. Yang, P. K. Chu and X.-F. Yu, *J. Phys. Chem. Lett.*, 2020, **11**, 1052–1058.
67 S. Wang, L. Shi, X. Bai, Q. Li, C. Ling and J. Wang, *ACS Cent. Sci.*, 2020, **6**, 1762–1771.